The Role of Polarizability in the Interfacial Thermal Conductance at the Gold-Water Interface

Hemanta Bhattarai and Kathie E. Newman

Department of Physics,

University of Notre Dame, Notre Dame, Indiana 46556,

USA

J. Daniel Gezelter[a)]

Department of Chemistry & Biochemistry,

University of Notre Dame, Notre Dame, Indiana 46556,

USA

(Dated: 12 October 2020)

We have studied the interfacial thermal conductance, G, of the flat Au(111) - water interface using non-equilibrium molecular dynamics simulations. We utilized two metal models, one based on the embedded atom method (EAM), and one which includes metallic polarizability via a density-readjusting embedded atom method (DR-EAM). These were combined with three popular water models, SPC/E, TIP4P, and TIP4P-FQ to understand the role of polarizability on the thermal transport process. A thermal flux was introduced using velocity shearing and scaling reverse non-equilibrium molecular dynamics (VSS-RNEMD), and transport coefficients were measured by calculating the resulting thermal gradients and temperature differences at the interface. Our primary finding is that the computed interfacial thermal conductance between a bare metal interface and water increases when polarizability is taken into account in the metal model. Additional work to understand the origin of the conductance difference points to changes in the local ordering of the water molecules in the first two layers of water above the metal surface. Vibrational densities of states on both sides of the interface exhibit interesting frequency modulation close to the surface, but no obvious differences due to metal polarizability.

[a)]Electronic mail: gezelter@nd.edu

I. Introduction

Metal surfaces are highly polarizable because there are many mobile electrons with easy access to the conduction band. Conductors respond rapidly to external electric fields, and the potential at the surface remains close to zero due to the rearrangement of electrons, resulting in local polarization of the metal upon exposure to electric fields. This effect plays a vital role in interfacial properties when metals are in close contact with polar solvents. The local electric fields generated by the solvent polarizes the metal surface, and in turn, the polarized metal interacts with the polar solvent affecting its static and dynamic properties. At these interfaces, we expect that the dynamics of the polar solvent molecules will be influenced by the induced image dipoles in the metal. This effect should alter the rate of heat transfer from metal to polar solvent relative to non-polarizable interfaces.

The force fields for bulk metals that are normally used in molecular dynamics simulations are largely based on the embedded atom method (EAM).[1–8] Variants like the Finnis-Sinclair,[9,10] modified embedded atom method (MEAM),[11–16] and quantum Sutton-Chen[17,18] have all been widely used by the materials simulation community for work on bulk and nanoparticle properties,[19–21] melting,[22–24] fracture,[25,26] crack propagation,[27] and alloying dynamics.[28] One of the strengths common to all of the methods is the relatively large library of metals for which these potentials have been parameterized.[2,29–37] However, the unmodified models do not allow the metal atoms to polarize, making them poor candidates to simulate interfaces involving a metal and a polar adsorbate.

Some efforts have been made to incorporate polarization into these models. The Electrostatic + EAM (ES+) model[38] is modification of the Finnis-Sinclair variant of EAM[9] which combines a variable-charge electrostatic approach with the EAM. Charge-equalization approaches based on the extended Lagrangian charge equalization method pioneered by Rick, Stuart, and Berne[39–41] have also been utilized to parametrize similar EAM+Charge Transfer models.[42–45] Zhou *et al.* modified EAM to include a charge transfer ionic-embedded atom method potential.

Although the above models add a degree of polarizablity to metals, these are largely tuned to replicate bulk-like properties for fully or partially oxidized metals, and not for surface interactions and screening at metal interfaces. Recently, we introduced a modification of the embedded atom method which allows for electronic polarization of the metal by treating the valence density around each atom as a fluctuating dynamical quantity. The densities are represented by a set of additional fluctuating variables (and their conjugate momenta) which are propagated along with

the nuclear coordinates. This "density readjusting EAM" (DR-EAM) preserves nearly all of the useful qualities of traditional EAM, including bulk elastic properties and surface energies.[46] It also allows valence electron density to migrate through the metal in response to external perturbations. DR-EAM can successfully model polarization in response to external charges, capturing the image charge effect in atomistic simulations. DR-EAM also captures some of the behavior of metals in the presence of uniform electric fields, predicting surface charging and shielding internal to the metal. It can also predict charge transfer between the constituent atoms in alloys, leading to novel predictions about unit cell geometries in layered $L1_0$ structures, most notably in NiPt.

There have also been recent molecular dynamics studies of heat conduction between nanoparticles and non-polar solvents.[47–49] Recently, Rajabpour *et al.* used molecular dynamics to study interfacial thermal transport at the nanoparticle-water interface.[50] However, these simulations are missing polarizablity, which should plays integral role in structure and dynamics of polar solvents in the vicinity of metal surface. In this paper, we seek to understand how large a role this effect has on this transport property. We report on the interfacial thermal conductivity of the gold and water interface using both unpolarizable (EAM) and polarizable (DR-EAM) models for the metal interacting with three distinct water models (SPC/E, TIP4P, TIP4P-FQ). The dependence of structural properties on the polarizability at the interface will also be investigated.

II. Simulating Metals in Contact with Polar Solvents

1. Polarizable and non-polarizable forcefields for metals

The interactions interior to the gold slab are modeled using both the embedded atom method (EAM) and density readjusting embedded atom method (DR-EAM).[37,46] EAM is non-polarizable forcefield for metals where the potential energy is a function of atomic coordinates $\{\mathbf{r}\}$,

$$V(\{\mathbf{r}\}) = \sum_i F_i[\bar{\rho}_i] + \frac{1}{2}\sum_i \sum_{j\neq i} \phi_{ij}(r_{ij}). \tag{1}$$

Here $F_i[\bar{\rho}_i]$ is an energy functional for embedding atom i in a total valence density, $\bar{\rho}_i$, located at $\mathbf{r}_i$, the position of the pseudo-atom i (nucleus + core electrons). ϕ_{ij} is a pair potential that represents the (mostly) repulsive overlap of the two pseudo-atom cores at a distance $r_{ij} = \left|\mathbf{r}_j - \mathbf{r}_i\right|$. In this paper we have adopted the parameters from Zhou *et al.*[37] EAM has been used for many properties of bulk metals as it captures the many-body interaction present in real metals. However, it lacks an important physical property, polarizablity.

Because water has a permanent dipole moment, the response of a metal surface adjacent to water molecules is expected to play a vital role in the heat transfer. To capture the effect of dipole-metal interaction at the gold-water interface, DR-EAM was also used in this paper. DR-EAM is polarizable force field for metal built on EAM. In DR-EAM, a collection of atoms with instantaneous positions, $\{\mathbf{r}\}$, and partial charges, $\{q\}$, has a configurational potential energy given by

$$V(\{\mathbf{r}\},\{q\}) = \sum_i F_i\left[\bar{\rho}_i\right] + \frac{1}{2}\sum_i\sum_{j\neq i}\phi_{ij}(r_{ij},q_i,q_j) + \frac{1}{2}\sum_i\sum_{j\neq i} q_i q_j\, J\left(r_{ij}\right) + \sum_i V_{\text{self}}\left(q_i\right). \tag{2}$$

Here, $F_i\left[\bar{\rho}_i\right]$ is the same (EAM) energy functional for embedding atom i in a total valence density, $\bar{\rho}_i$, located at $\mathbf{r}_i$. ϕ_{ij} is a pair potential that represents the (mostly) repulsive overlap of the two pseudo-atom cores at a distance $r_{ij} = \left|\mathbf{r}_j - \mathbf{r}_i\right|$, but which is also the function of partial charges on respective atoms. $J\left(r_{ij}\right)$ is the Coulomb integral that accounts for electrostatic contributions from the fluctuations in the valence-charge density distributions, and V_{self} is the energy for under- or over-charging each atom.

The instantaneous electron density due to the valence electrons from all the other atomic sites is computed at the location of each atom. For atom i,

$$\bar{\rho}_i = \sum_{j\neq i}\left(1 - \frac{q_j}{N_j}\right) f_j\left(r_{ij}\right), \tag{3}$$

where $f_j(r)$ is the radial dependence of the valence density of neutral atom j, and q_j is a dynamic charge variable that governs the instantaneous fluctuations in the valence density. N_j is a "valency count" for atom j that is determined by the number of free charge carriers in the bulk metal. Changes in the partial charge value allow for conduction band electrons ($q < 0$) or holes ($q > 0$) to migrate into a spatially localized cloud surrounding each atom.

The pair potential, ϕ_{ij}, in DR-EAM also depends on the instantaneous valence densities at sites i and j.

$$\phi_{ij}\left(r,q_i,q_j\right) = \frac{1}{2}\left[\frac{f_j(r)\left(1-\frac{q_j}{N_j}\right)}{f_i(r)\left(1-\frac{q_i}{N_i}\right)}\phi_{ii}(r) + \frac{f_i(r)\left(1-\frac{q_i}{N_i}\right)}{f_j(r)\left(1-\frac{q_j}{N_j}\right)}\phi_{jj}(r)\right], \tag{4}$$

where ϕ_{ii} is the pair interaction of two i atoms in the pure bulk metal.

A treatment of electrostatic interactions is required to account for local perturbations to the background electron density. In the simulations described here, we have adopted the damped

shifted force (DSF) kernel,[51]

$$J(r) = \left[\frac{\mathrm{erfc}\,(\alpha r)}{r} - \frac{\mathrm{erfc}\,(\alpha R_\mathrm{c})}{R_\mathrm{c}} + \left(\frac{\mathrm{erfc}\,(\alpha R_\mathrm{c})}{R_\mathrm{c}^2} + \frac{2\alpha}{\pi^{1/2}} \frac{\exp\left(-\alpha^2 R_\mathrm{c}^2\right)}{R_\mathrm{c}} \right)(r - R_\mathrm{c}) \right] \quad r \leqslant R_\mathrm{c}, \tag{5}$$

which has energies and forces that go smoothly to zero approaching a cutoff value, R_c. The damping parameter, α, describes the effective screening length of the charge, essentially treating density perturbations as Gaussians of width α^{-1}.

The self potential, V_self, in DR-EAM accounts for the energetic penalty for over-charging or under-charging a neutral atom, and is modeled with a polynomial,[52]

$$V_\mathrm{self}(q) = \sum_{n=1}^{6} a_n\, q^n. \tag{6}$$

The parameters have been tuned using a range of electron affinities and ionization potentials for commonly exhibited oxidation states in bulk materials. All of the parameters for DR-EAM can be found in Ref. 46.

2. Polarizable and Non-polarizable solvent models

The water models used in the simulations include both polarizable and fixed-charge water models. The fixed-charge models include SPC/E[53] and TIP4P.[54] The dipole moment is fixed in SPC/E and TIP4P, with water represented by 3 and 4 sites, respectively. We utilized TIP4P-FQ as our polarizable water model, where the partial charges on the charge carrying sites may fluctuate in response to changes in the surrounding environment.[39] The Coulombic and self potential in TIP4P-FQ allow the charge degrees of freedom to move slowly on an energy surface that is largely harmonic. TIP4P-FQ reproduces the gas-phase dipole moment, energy, and rotational diffusion constants of experiments.[39] It is an intriguing model to study heat transfer as the coupling of the charge oscillation could play a significant role in the structural and dynamical properties of both the bulk liquid and interface.

3. Cross-interactions between the metal and solvents

Development of an interaction potential for metal-water systems started with one originally proposed by Spohr which was modified significantly by Dou *et al.* to study explosive boiling

of water adjacent to heated metal surfaces.[55] In the Dou *et al.* modification, the Metal-Oxygen interaction is treated with a Morse potential and Metal-Hydrogen interactions are treated using purely repulsive (exponential) potentials,

$$V_{\mathrm{MO}}(r_{\mathrm{MO}}) = D_0 \left[e^{-2\beta_O (r_{\mathrm{MO}} - r_{e_1})} - 2e^{-\beta_O (r_{\mathrm{MO}} - r_{e_1})} \right] \tag{7}$$

$$V_{\mathrm{MH}}(r_{\mathrm{MH}}) = \gamma\, D_0\, e^{+2\beta_H (r_{\mathrm{MH}} - r_{e_2})}. \tag{8}$$

Here r_{MX} is the distance between metal and either the oxygen (X=O) or hydrogen (X=H) atoms. All other constants are parameters that can be found in Ref. 55.

In the Dou *et al.* model, the Metal-Oxygen and Metal-Hydrogen potentials are well defined for all separations, but when point charges are present on both the water sites *and* the metal atoms, there is a possibility of Coulombic divergence as $r \to 0$. For this reason, we modeled Metal-Oxygen interactions using a Mie potential,[56] and the Metal-Hydrogen interaction with an inverse power of distance,

$$V_{\mathrm{MO}}(r_{\mathrm{MO}}) = \left(\frac{n}{n-m}\right)\left(\frac{n}{m}\right)^{m/(n-m)} \epsilon_O \left[\left(\frac{\sigma_O}{r_{\mathrm{MO}}}\right)^n - \left(\frac{\sigma_O}{r_{\mathrm{MO}}}\right)^m \right] \tag{9}$$

$$V_{\mathrm{MH}}(r_{\mathrm{MH}}) = \epsilon_H \left(\frac{\sigma_H}{r_{\mathrm{MH}}}\right)^p \tag{10}$$

These functional forms prevent site-site overlap that results in unphysical divergences when point charges are used. The parameters of the cross interaction were tuned to match the Dou *et al.* model as closely as possible in the attractive well (see Fig. 1). The values of the parameters for the modified potential are listed in table I.

TABLE I: Parameters for the Metal-Water cross interaction in eqs. 9 and 10.

Parameter	m	n	ϵ_O (eV)	σ_O (Å)	p	ϵ_H (eV)	σ_H (Å)
Value	9	6	6.81×10^{-2}	3.182	4	9.21×10^{-5}	1

This potential produces H_2O-Au(111) binding energies (table II) that are reasonably close to the 0.455 eV binding energy reported by Dou *et al.* Note that the electrostatic interactions in DR-EAM play a relatively small role in the binding energetics, but they may alter binding site and orientational preference at the surface. The different partial charge values on the three water models have little effect on the binding energies.

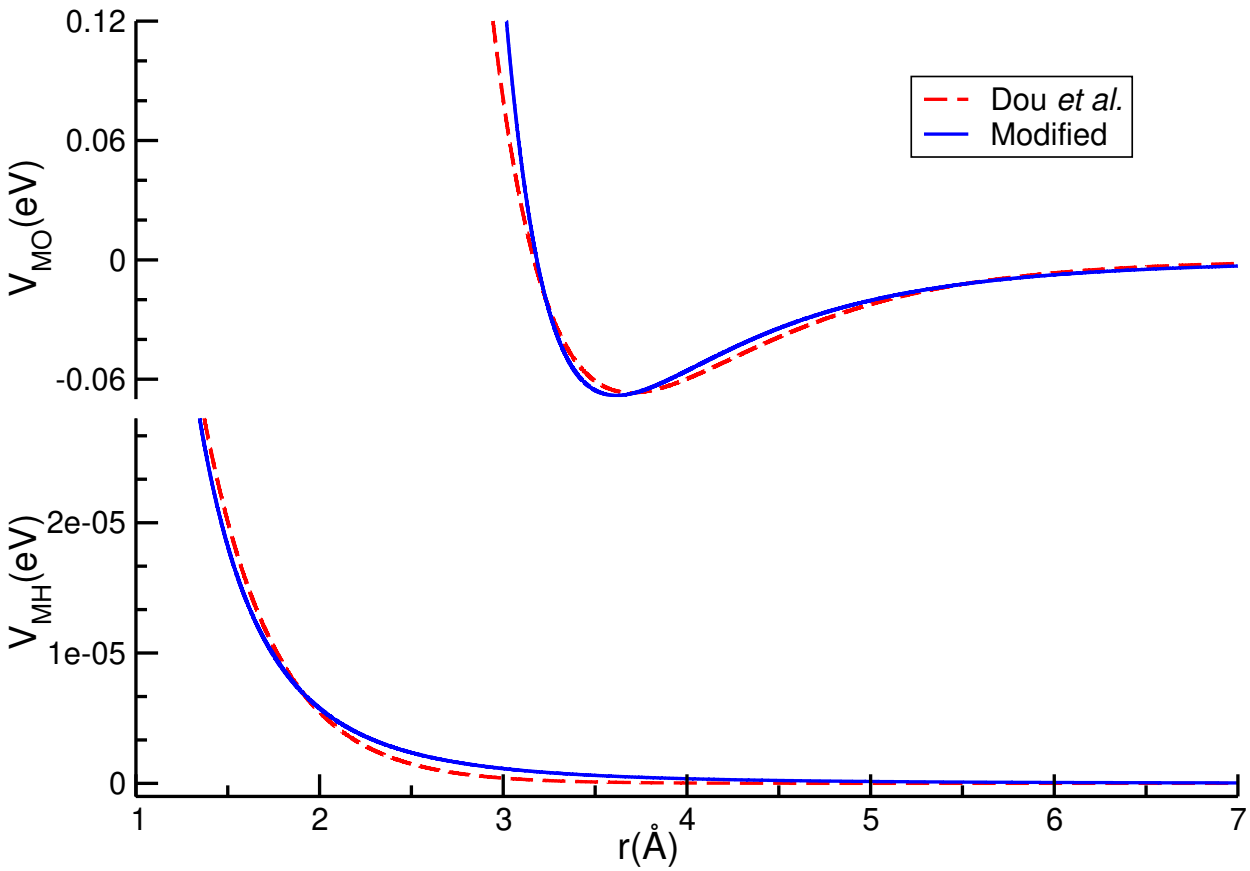

FIG. 1: Comparison of the interaction potentials of Dou *et al.* (Ref. 55) and the cross potential used in this work. Top: Gold-Oxygen interactions. Bottom: Gold-Hydrogen interactions.

TABLE II: Binding energy (in eV) for a single water molecule on surface of gold (111)

	EAM	DR-EAM
SPC/E	0.537	0.542
TIP4P	0.537	0.542
TIP4P-FQ	0.537	0.542

A. Creating non-equilibrium thermal gradients

Calculating bulk transport properties is one of the main uses of equilibrium molecular dynamics (EMD) simulations. Many transport coefficients (e.g. diffusion, viscosity, thermal conductivity) can be computed using Green-Kubo formulas by integrating the appropriate flux autocorrelation functions obtained via EMD.[57] However, these functions often become noisy at longer times, and

slow transport processes require both long simulations and relatively frequent storage of system configurations to converge, making this approach prohibitive in larger systems.

One solution is to utilize Non-Equilibrium Molecular Dynamics (NEMD) simulations, where the system is perturbed from equilibrium and the response is used measure transport properties. NEMD algorithms create gradients in momentum or kinetic energy and calculate the resultant flux to arrive at the transport coefficients. However, imposing gradients and measuring the flux, particularly for interfacial systems, presents many challenges. Reverse Non-Equilibrium Molecular Dynamics (RNEMD) methods have been developed where the non-physical flux is applied to the system and the system attains steady state gradients in response. Gradients are relatively easy to measure and transport coefficients can be calculated effectively.[58] The first variant of technique, developed by Müller-Plathe, has molecules in hot and cold bins swap their momentum vectors to create the non-physical flux. Momentum swaps can disturb the Maxwell-Boltzmann distribution of velocities, so in this paper all of the non-equilibrium molecular dynamics simulations are done using the Velocity Shearing and Scaling Reverse Non-Equilibrium Molecular Dynamics (VSS-RNEMD) technique, which preserves Maxwell-Boltzmann distributions of velocities.[59] In VSS-RNEMD, a non-physical flux is applied to the system, and the shearing and scaling parameters are obtained by solving the conservation equations for both linear momentum and energy. At steady state, a temperature gradient can be obtained for each applied flux. Using the calculated temperature gradient and applied kinetic flux, transport coefficients like the thermal conductivity and interfacial thermal conductance can be easily calculated.

During RNEMD simulations, thermal gradients (∇T) develop inside bulk materials, while temperature differences (ΔT) develop at the interfaces between materials. These allow straightforward calculation of thermal conductivities ($\lambda_{\text{solid}}, \lambda_{\text{liquid}}$) and interfacial thermal conductance (G) values (see Fig. 2).

B. Simulation Protocol

In this paper we are studying the gold-water interface, where gold is modeled using EAM and DR-EAM and water is modeled using SPC/E, TIP4P and TIP4P-FQ. There are six systems of interest, *i.e.*, every possible combination of gold and water models. The system contains 3125 water molecules and 1800 gold atoms. The gold slab with exposed (111) surfaces is sandwiched between water. The dimensions of the system is 29.89 Å× 28.84 Å× 148 Å. All the systems

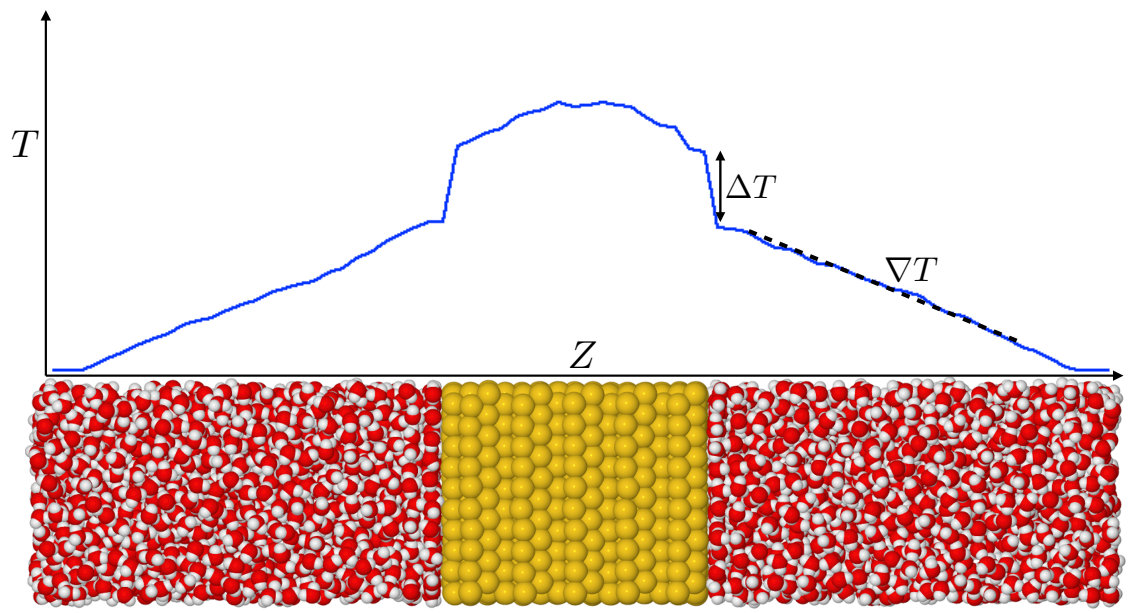

FIG. 2: A representative temperature profile along the z axis that develops during an RNEMD simulation of a gold / water interface. Under constant thermal flux, material properties of both the solid and liquid regions, as well as interfacial properties can be computed by looking at the regional dependence of the thermal profile.

have the same thermodynamics state, *i.e.*, the same temperature and pressure of 300 K and 1 atm. Prior to the data collection runs, the velocities, both linear and angular, are re-scaled such that the temperature on both sides of the interface is 300K. For RNEMD runs, a non-physical thermal flux of 2.5 $\times 10^{-6}$ kcal mol^{-1}Å^{-2}fs^{-1} is used for interfacial systems, with momentum exchanges between the two RNEMD regions carried out every 1.0 fs for the systems containing polarizable models, and every 2.0 fs for those without. After steady state is reached, the temperature difference between the hottest bin (in gold) and coldest bin (in water) is about 15K and density of the water is fairly constant in the region containing water.

III. Results

A. Bulk Thermal Conductivity of Water

The bulk thermal conductivity of a material is a measure of its ability to conduct heat. The thermal conductivity is defined through a linear constitutive relation (Fourier's Law) relating the

heat flux $\mathbf{J}$ to the gradient of the temperature,

$$\mathbf{J} = -\lambda \nabla T. \tag{11}$$

When steady state is reached during a reverse non-equilibrium molecular dynamics (RNEMD) simulation, the thermal flux is a non-physical applied quantity, and the temperature gradient is measured in the simulation cell. A simple linear fit of the temperature profile in the regions unperturbed by the RNEMD exchange moves yields an estimate of ∇T. The thermal conductivity is then related to the magnitude of the applied thermal flux.

Jia *et al.* have shown that simulated thermal conductivities have a system size dependence, *i.e.*, the value of λ depends on the physical length of the simulation cell.[60] They found a relation between finite-size thermal conductivity values (λ), and the length of the box (L),

$$\frac{1}{\lambda} = \frac{1}{\lambda_\infty} + \frac{c}{L}, \tag{12}$$

where λ_∞ is the thermal conductivity projected to an infinite length cell, and c is a fitting constant that depends on the particular material. To compute the infinite-length limit of the bulk thermal conductivity, one needs to create a series of simulations of increasing length and then fit the particular λ vs. L relationship.

For each of the three water models, we simulated six different simulation cell lengths (with the same cross sectional area). These cells ranged in size from $29.89 \times 28.84 \times 40$ Å to $29.89 \times 28.84 \times 160$ Å. For each simulation cell, 5 statistically-independent RNEMD simulations (with $J_z = 4.0 \times 10^{-6}$ kcal mol^{-1}Å^{-2}fs^{-1}) were carried out in order to find linear J vs. ∇T relationships and to fit λ values.

The infinite-length limit of the bulk thermal conductivities for each model were computed using a linear least squares fit of the $1/\lambda$ vs. $1/L$ values to Eq.(12). The individual thermal conductivity estimates and the linear projections are shown in the Supplemental Material in Fig. S1. Our estimates of the infinite-length thermal conductivities for these water models are given in Table III.

The calculated values of the bulk thermal conductivity for SPC/E and TIP4P are similar to values reported by Römer, Lervik,and Bresme,[62] as well as those reported by Sirk, Moore, and Brown.[63] Of the three water models investigated, TIP4P comes closest to reproducing the experimental bulk thermal conductivity of water at 300K.[61]

TABLE III: Infinite-length limit of the calculated bulk thermal conductivities of different water models

Water Model	λ_∞(W m^{-1} K^{-1})
SPC/E	0.87 ± 0.05
TIP4P	0.79 ± 0.03
TIP4P-FQ	0.84 ± 0.03
Experiment (Ref. 61)	0.6096

B. Interfacial Thermal Conductance

Interfacial thermal conductance is a measure of how effectively heat transfers from one material to another at an interface. Under the influence of a thermal flux (J), two materials can exhibit a temperature difference (ΔT) at the location of the interface. This behavior is described by another linear constitutive relation,

$$J = G\Delta T \tag{13}$$

where G is the interfacial thermal conductance.

In RNEMD simulations, after the steady state temperature profile develops, the temperature difference at the interface is calculated, and using the magnitude of the applied thermal flux, the interfacial thermal conductance is easily computed.[59] Temperature differences, ΔT, are measured using the average local temperatures in 2Å spatial bins close to the interface. We use the first bin on either side that is unambiguously in the metal region, or unambiguously in the liquid region, *i.e.*, no population from the other side of the interface.

In this work, we used ten statistically-independent replicas of each Au(111) - water interface. Both non-polarizable (EAM) and polarizable (DR-EAM) models of the metal were used in combination with two non-polarizable (SPC/E, TIP4P) and one polarizable (TIP4P-FQ) water models. For each of the sixty simulations, after equilibration, the RNEMD data collection was carried out for 1 ns. Interfacial temperature jumps (ΔT) were computed over the duration of the data collection portion, and these were used to calculate the interfacial thermal conductivities using Eq. (13). Computed interfacial thermal conductivities are given in table IV. The statistical error in the computed values of G is due largely to fluctuations in ΔT at the interface. In the VSS-RNEMD method, J is an imposed quantity, with very little noise. For moderate flux values, mean ΔT values

at the metal/water interface are approximately 6 K, depending on water model, while the standard error for measuring ΔT are approximately 0.4 K. The metal/water interface also has a very large conductance, so ΔT values are relatively small compared with metal/alkane interfaces,[64] and the reported errors in G are significantly larger. Reducing fluctuations in ΔT would require simulations that increase the lateral surface area of the interface.

TABLE IV: Calculated interfacial thermal conductivities (G) of the Au(111) - water interface (in MW m^{-2} K^{-1}) simulated using different force fields for both gold and water.

	metal model	
water model	EAM	DR-EAM
SPC/E	254 ± 17	279 ± 16
TIP4P	301 ± 23	329 ± 32
TIP4P-FQ	277 ± 20	291 ± 19

In all cases studied, the addition of charge degrees of freedom in the DR-EAM model enhances the interfacial thermal conductivity at metal/water interface. The charges on the metal atoms provide an effective coupling between metal atom motion and motion in the water even for fixed charge models like SPC/E and TIP4P.

For the fluctuating charge water model (TIP4P-FQ) there is an additional direct coupling between the charge degrees of freedom on both sides of the interface. However, in water, the polarizability of TIP4P-FQ lowers the conductance at the interface relative to the similar TIP4P model. One explanation for this observation is that TIP4P-FQ has a lower *bulk* thermal conductivity (see table III above), and λ is important in pulling heat away from the interface. Additionally, we note that average partial charges in TIP4P-FQ are typically larger than the fixed charges in TIP4P, so enhanced polarization of the liquid may be playing a role here.

One of the more pressing questions is the role of surface polarizability in ordering the structure of water at the surface, as this could change the dynamical behavior of the near-surface liquid. In the next section, we turn our attention to the behavior of water molecules and metal atoms that are close to the interface. We thus look for differences in behavior in the six models examined (SPC/E, TIP4P, and TIP4P-FQ for water with either EAM or DR-EAM for the metal).

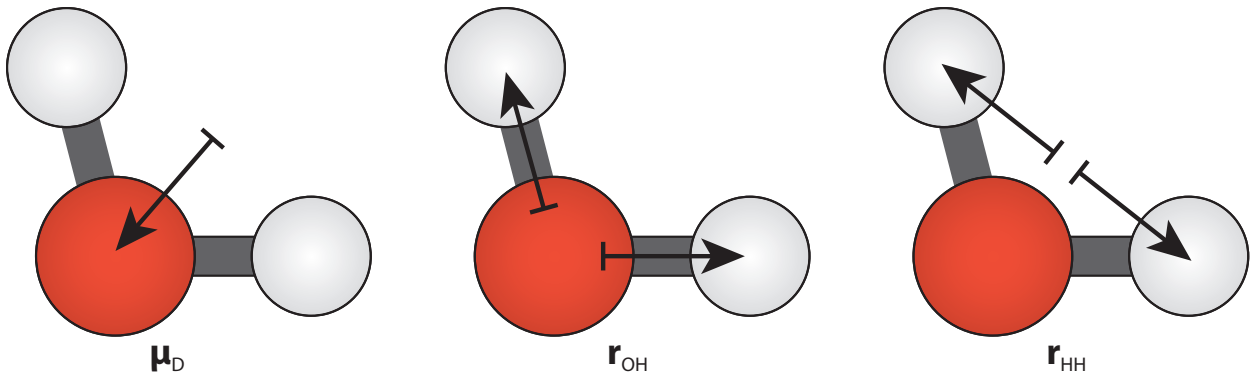

FIG. 3: Unit vectors associated with the frame of each water molecule that were used in determining orientational ordering relative to the interface normal. Note that for the OH bond vectors, each water molecule has two contributions, and for the HH interatomic vector, two vectors contribute to the population distributions.

C. Water Behavior at the Interface

Quantitative measurement of the structural ordering of water was carried out using a set of orientation parameters for molecular vectors (dipole, OH bond vector, HH vector) for the molecular frame of water (see Fig. 3). These particular molecular vectors were chosen to show the role of the electrostatic dipole in orienting the water.

Each of these vectors can be projected onto the interface normal vectors, $\hat{\mathbf{z}}$ or $-\hat{\mathbf{z}}$, providing a single angle (θ) which describe each of the vectors on the water molecules. If the dipole direction is given by a vector $\hat{\mu}_D$, then the pitch of the dipole vector towards the surface is denoted by an angle θ_D. Similarly, θ_{OH} and θ_{HH} are used for the directions of the OH bonds and for the interatomic HH vector interior to each water molecule.

For each type of angle θ, there are two obvious choices of orientational order parameters, the first-order $\langle P_1(\cos\theta)\rangle$ and second-order $\langle P_2(\cos\theta)\rangle$ Legendre polynomials:

$$S_1 = \langle P_1(\cos\theta)\rangle = \langle\cos\theta\rangle \tag{14}$$

$$S_2 = \langle P_2(\cos\theta)\rangle = \frac{3\langle\cos^2\theta\rangle - 1}{2} \tag{15}$$

where S_2 is expected to be most relevant for symmetric vectors (e.g. the HH vector, and S_1 is most useful for asymmetric vectors (e.g. the molecular dipole). Note that S_1 and S_2 are distinct for each of the molecular-frame vectors ($\hat{\mu}_{\mathrm{D}}, \hat{\mathbf{r}}_{\mathrm{OH}}, \hat{\mathbf{r}}_{\mathrm{HH}}$).

In Fig. 4, the spatially-resolved dipolar orientational order parameters show only modest differ-

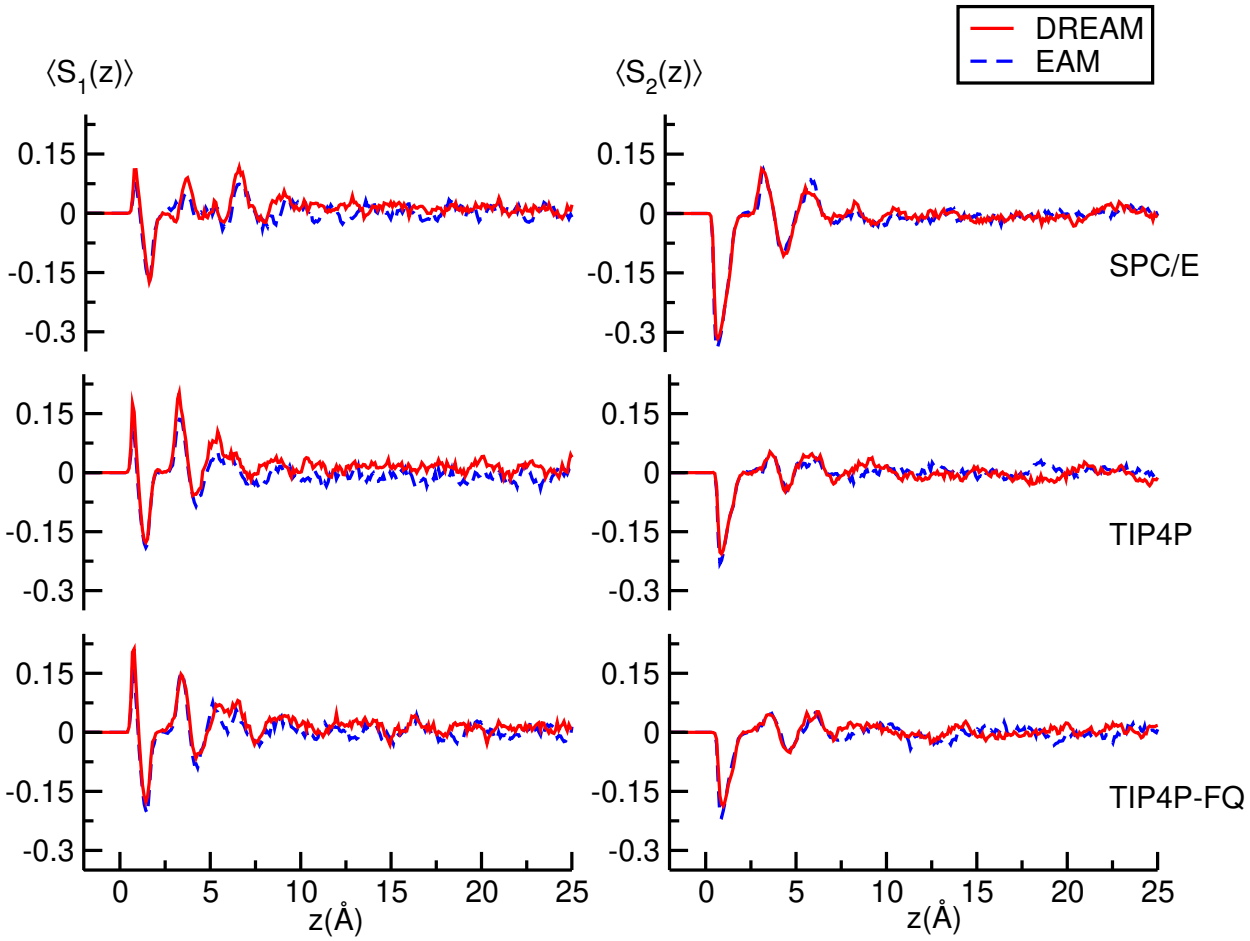

FIG. 4: Comparison of the spatially-resolved mean dipole orientational order parameters, $\langle S_1(z)\rangle$ and $\langle S_2(z)\rangle$ for three different water models (SPC/E, TIP4P, TIP4P-FQ) and two models for the metal (EAM and DR-EAM).

ence between polarizable (DR-EAM) and non-polarizable (EAM) models for the metal. We note that all water models display enhanced ordering near the metal surface (reflected in the alternating peaks in S_1), with the TIP-based models exhibiting ordering out to the second layer above the surface (set to the reference $z = 0$ Å in this figure). There do appear to be some residual differences between DR-EAM and EAM in the TIP4P model at larger distances from the surface, but it is not clear how that would alter heat transfer at the interface.

Two types of figures are used to look the population of water molecules that have particular orientation vectors. In the Supporting Information, Figs. S2, S3, and S4 illustrate these distributions as heat maps for the water dipole vector, OH bond vectors, and HH interatomic vector, as a function of distance from the surface, respectively. The heat maps represent the proportion of the

water molecules with a specific combination of $(\cos\theta_D, z)$, $(\cos\theta_{\mathrm{OH}}, z)$, and $(\cos\theta_{\mathrm{HH}}, z)$ and show data for the first four layers of water away from the surface of the metal. Figures 5, 6, and 7 show two cuts in the distance z for this data for the first- and second-layer distances from the interface. These figures have the population distribution shown as a function of the appropriate $\cos\theta$ and thus highlight more clearly differences between the six models studied.

First, we call attention to the nature of the water ordering seen for SPC/E water models. From Fig. 5, we see that the water dipoles in the first layer orient mostly parallel to the interface ($\cos\theta_D \sim 0.25$), with a second population ($\cos\theta_D \sim -0.7$) preferring a hydrogen up orientation. In the second layer we see a peak in θ_D at around ($\cos\theta_D \sim +0.75$. We interpret this to mean that the water molecules in the second layer are in the hydration shell of water molecules directly on the surface, and they are adopting orientations that enable hydrogen bonding to the horizontal molecules on the surface.

The two TIP models show a slightly different dipolar ordering than in SPC/E, preferring two distinct orientations on the surface, one that is mostly horizontal, but in one with the oxygen pointed down. Hexagonal rings of 6 water molecules are expected to display this ordering as three members of the ring have axial hydrogen, while three have equatorial hydrogens. In the second water layer, the three water models exhibit similar orientational preferences.

Next, we examine the differences between the two types of metal models, EAM and DR-EAM. Although the differences in water dipole orientation are small between DR-EAM and EAM, all three water models show an increase in the population of oxygen-up orientations ($\cos\theta_D = 0.75$) relative to non-polarizable metals.

In the supplementary material, Fig. S2 shows the population distribution as a function of distance from the interface (a more comprehensive picture than Fig. 5). Similar observations may be drawn from this data as well.

Water molecules can also orient to point OH bonds either towards ($\cos\theta_{OH} = -1$) or away ($\cos\theta_{OH} = +1$) from the surface. For local negative charge distributions in the metal, the OH bond will point directly at the location of that charge. Fig. 6 demonstrates this point. SPC/E shows a distinct pattern relative to the TIP models, which prefer their waters to have one Hydrogen parallel to the plane, and the other in an H-down or H-up configuration. SPC/E water at the surface is dominated by configurations with a HH vector parallel to the surface normal, giving two distinct peaks in the OH ordering (see also the following figure). By the second layer of water, most of the distinguishing characteristics between the water models have been washed out.

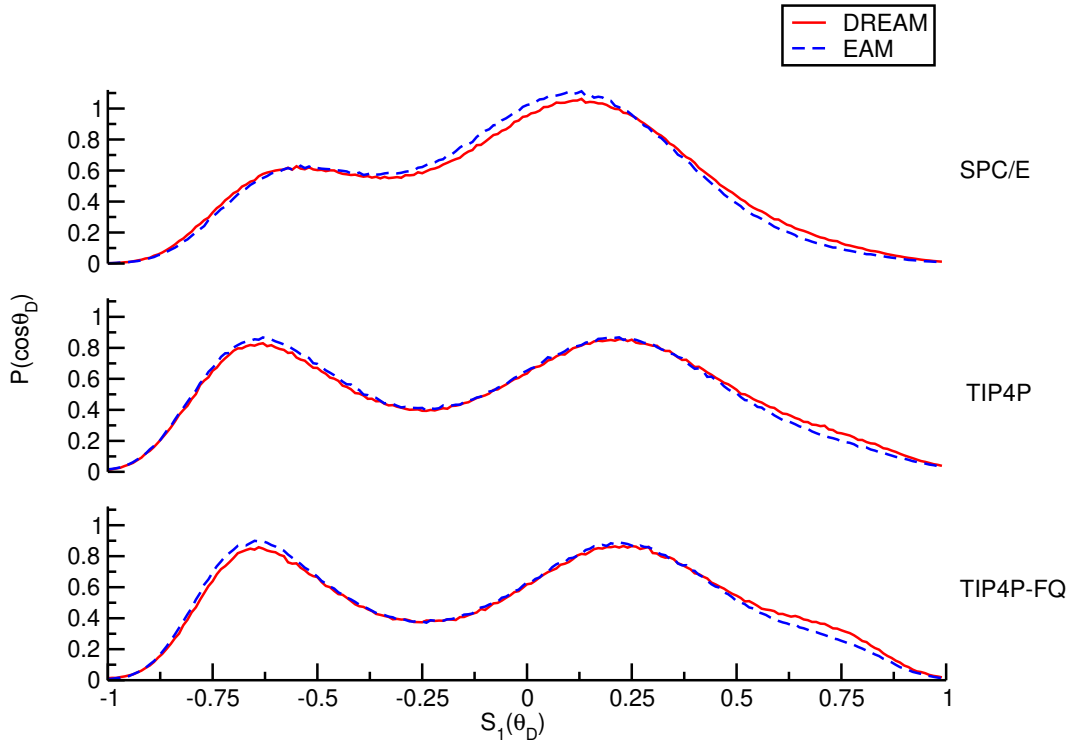

(a) First layer

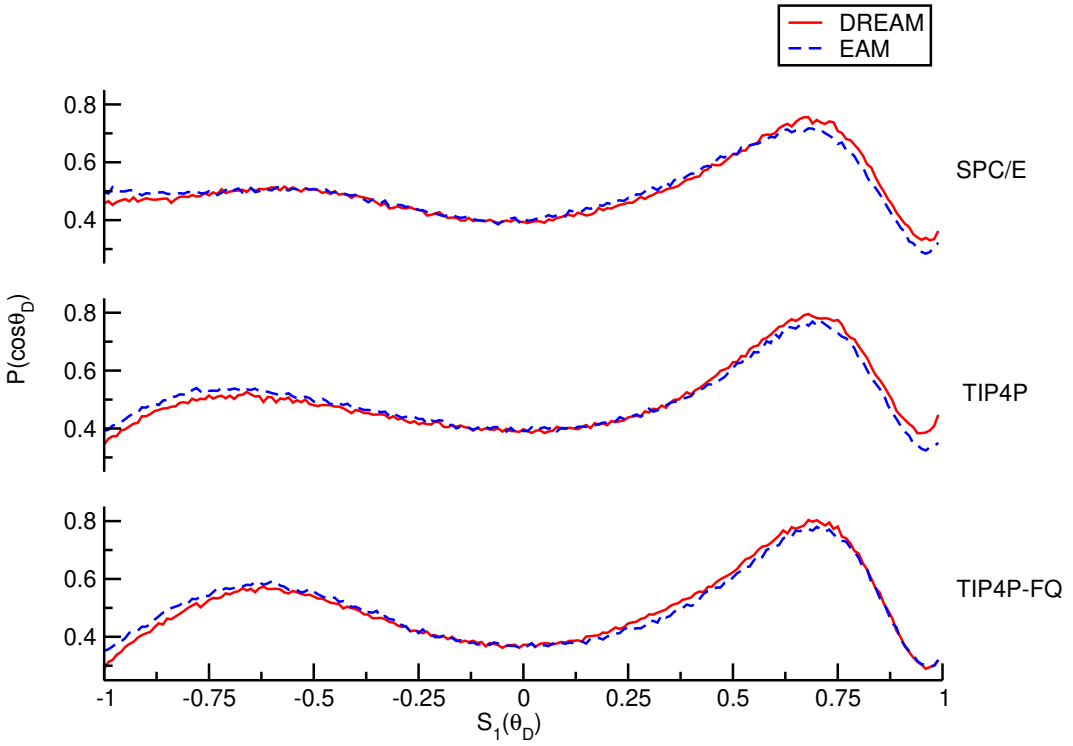

(b) Second layer

FIG. 5: The probability distribution, $P(\cos\theta_D)$, for water molecule dipoles in the first two layers adjacent to the metal surface. Each curve represents a configurational average of the water molecules in the $0-3$ Å and $3-6$ Å ranges above the surface.

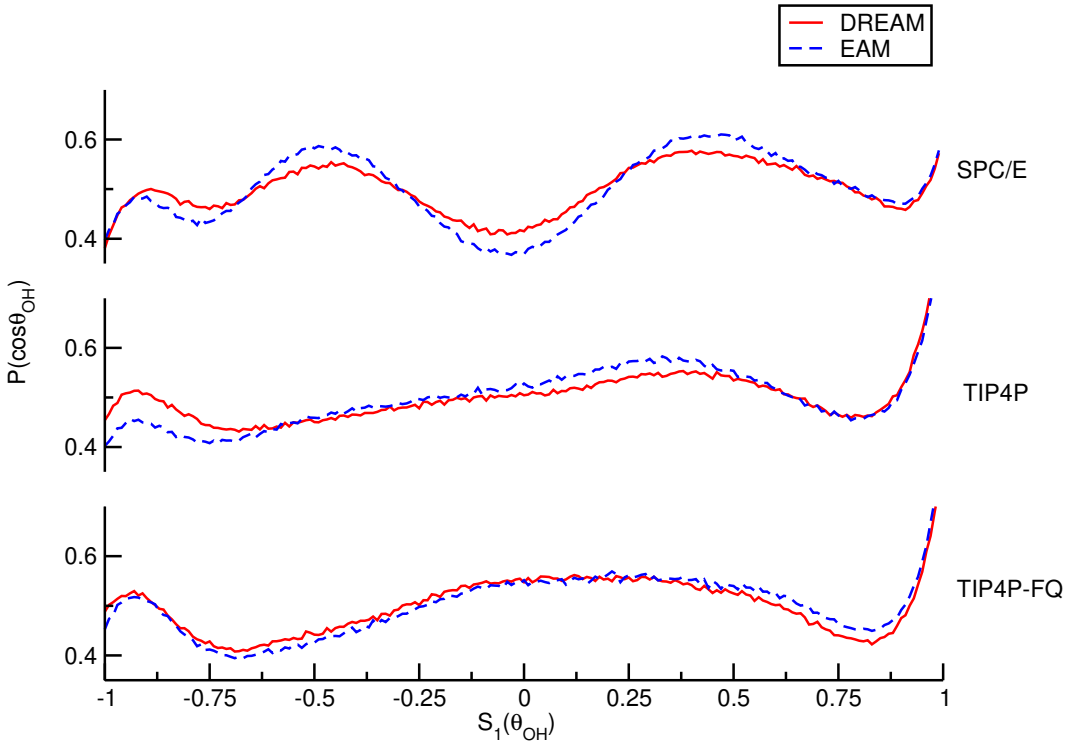

(a) First layer

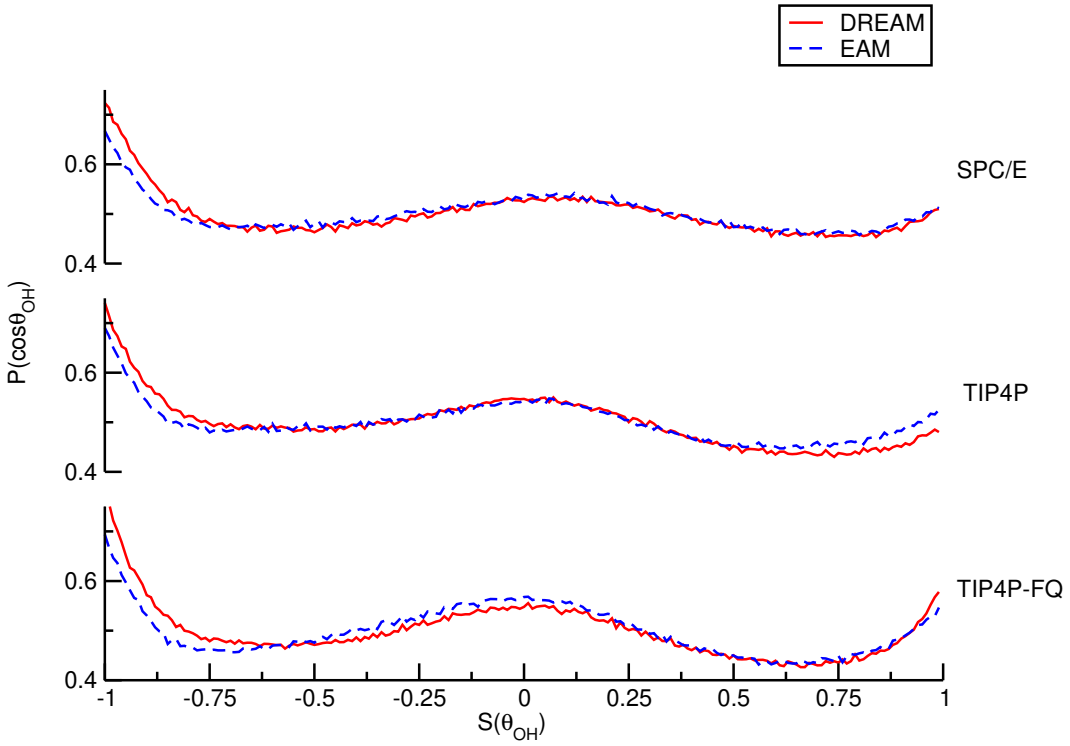

(b) Second layer

FIG. 6: The probability distribution, $P(\cos\theta_{OH})$, for OH bonds in water in the first two layers adjacent to the metal surface. Each curve represents a configurational average of the water molecules in the $0-3$ Å and $3-6$ Å ranges above the surface.

In the supplementary material, Fig. S3 shows the same population distribution as a function of distance from the interface, yielding similar observations.

Although it is a subtle effect, when the metal model is changed from EAM to DR-EAM, the distributions of OH angles in the first water layer are flattened. This indicates that the polarizability in DR-EAM permits a wider range of water orientations at the surface. In contrast, metal polarizability seems to enhance the H-down preference in the second layer of water.

Turning our attention to the HH interatomic vector, we note that there are differences in the water ordering that depend on the polarizability of the metal (see Fig. 7). Specifically, DR-EAM tends to enhance the HH orientations parallel to the surface normal in the first water layer relative to the non-polarizable model. For TIP4P-FQ, the effect is most pronounced in the second layer of water, as the first shows very little dependence on the polarizability.

In the supplementary material, Fig. S4 shows the same population distribution as a function of distance from the interface, yielding similar observations.

In combination with the dipolar and OH bond ordering, we can gain a more complete picture of the water ordering at the surface. For SPC/E, the dipoles are roughly parallel to the surface, while the OH bond vectors show a strong preference for orientations that point one of the OH bonds towards the surface, and the HH vector directly perpendicular to the plane of the surface. For the TIP-based models, there is also a clear preference at the interface for one H pointed parallel to the interface, while the second hydrogen is pointed away from the surface. For the second layer, one H is pointed directly at the interface. Bilayer structures in ice have similar alternating OH bond vectors between adjacent layers.

Adding polarizibility to the metal causes local changes in water orientational ordering at the surface. These changes are quite subtle, but differences in the distributions of the three water vectors indicate that these changes are measurable. This structural picture is one possible explanation of altered thermal conductivity at the surface. Changes in water orientational ordering and added electrostatic coupling will alter the forces felt by metal and water atoms that are in direct contact with each other.

D. Vibrational Density of States

We examine now the behavior of metal atoms as a function of the distance z beneath the surface. The metal remains crystalline and has no orientational degrees of freedom. However, one measure

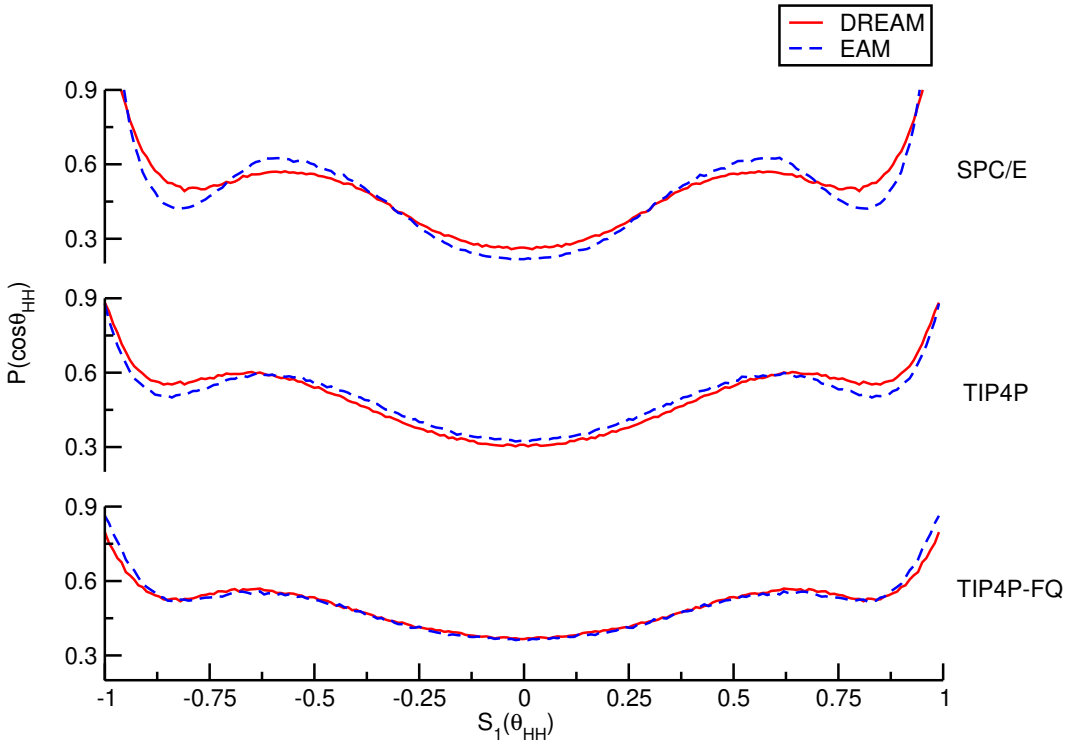

(a) First layer

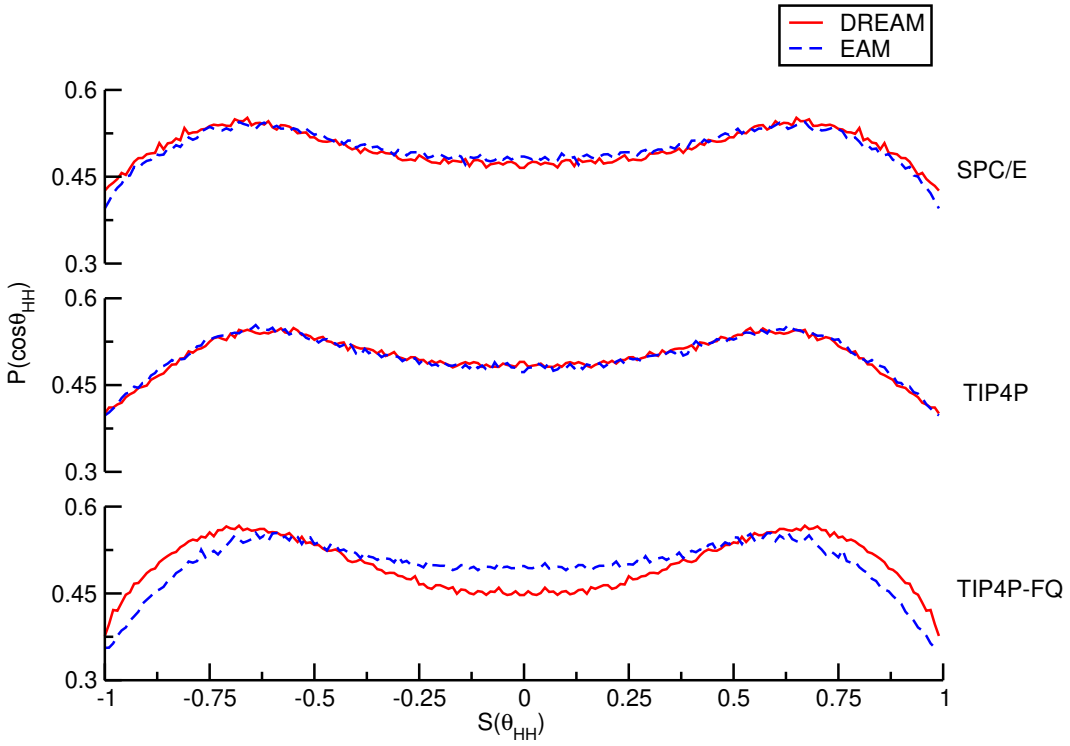

(b) Second layer

FIG. 7: The probability distribution, $P(\cos\theta_{HH})$, for interatomic HH vectors inside each water molecule. This data is collected for the first two layers of water adjacent to the metal surface.

of conformational freedom that can change as a function of z is the vibrational density of states, which closely mimics the phonon spectrum. Surface phonons in metals are different than those in bulk. An examination of the metallic density of states as functions of the frequency ω and interfacial distance z will capture some of these differences. Additionally, the various water models may show different phonon density of states as a function of the distance from the interface z. As was the case in the previous subsection, results can be shown both as population/heat maps as a function of z as well as plots of the same information as a function of ω for different regions away from the interface.

Fig. 8 shows the vibrational density distribution,

$$\rho(\omega, z) = \int_{-\infty}^{\infty} \langle \mathbf{v}(t, z)\mathbf{v}(0, z)\rangle e^{-i\omega t} dt \tag{16}$$

in metal and water for all 6 combinations of models. Details of how this is computed are included in the Supplemental Material. Fig. S6 shows that the distribution of frequencies is similar for all combinations of metal and water models. In the metal, the population of mode frequencies shifts overall to lower frequencies, favoring the longitudinal band near 60 cm^{-1} while the transverse band near 110 cm^{-1} bends higher in frequency near to the surface. On the water side, the peak in the vibrational density of states in layers near the surface shifts towards higher frequencies than the bulk density of states.

IV. Discussion

Our primary finding is that the computed interfacial thermal conductance between a bare metal interface and water increases when polarizability is taken into account in the metal model. We come to this conclusion via non-equilibrium molecular dynamics simulations of the thermal transport process, where the only differences between the series of models is the treatment of polarizability.

As seen in the previous section, the vibrations exhibited on either side of the interface bend towards higher frequencies close the interface (although in the metal, the lower frequency longitudinal modes dominate the population). However, there are no noticeable changes in these densities of states when going from a non-polarizable to polarizable model (for either the metal or water). The larger change is found in the ordering of the water phase, which slightly prefers hydrogen-down orientations near polarizable metals.

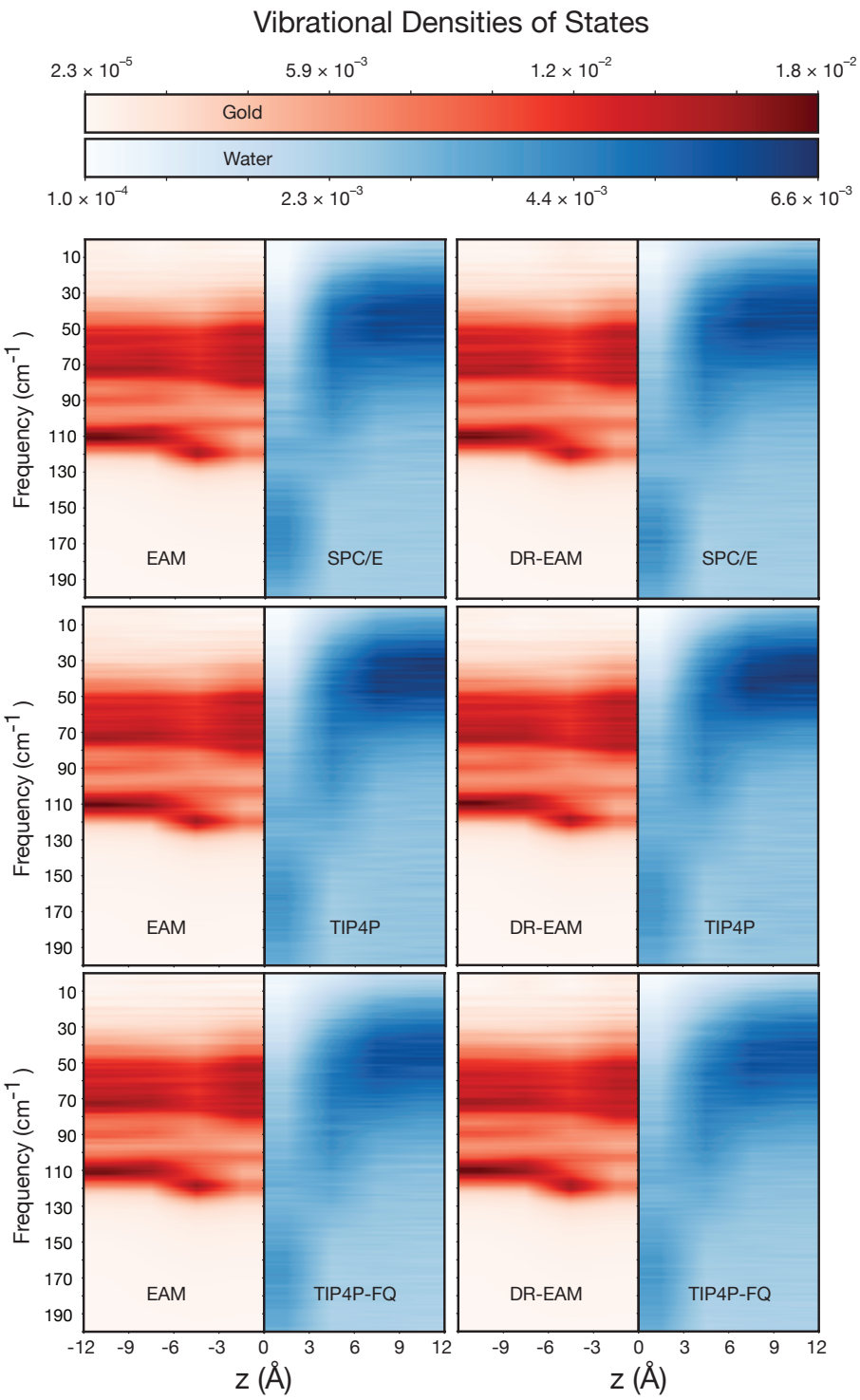

FIG. 8: An illustration of the localized vibrational density of states for atoms located in a 3 Å range around each value of z. The vertical (frequency) axis denotes the vibrational frequency, while the intensity of the color shows the relative fraction of vibrational states at that frequency. The two sides of each figure (separated at $z = 0$) show the metal (on the left) and the water (on the right).

To help understand this effect, we can revisit the various mismatch models for interfacial thermal transport between two materials a and b,

$$G_{ab} = \frac{1}{4\pi} \sum_p \int \int \int \hbar\omega \frac{\partial f}{\partial T} v_a(\omega, p) \rho_a(\omega, p) \tau_{ab}(\omega, p) \cos\theta \sin\theta d\theta d\phi d\omega \tag{17}$$

where f is the Bose-Einstein distribution function, $v_a(\omega, p)$ is the group velocity (on side a) for a phonon characterized by frequency ω, moving in direction (θ, ϕ) with polarization p. The relevant material properties are the density of phonon states, $\rho_a(\omega, p)$ and the transmission probability, $\tau_{ab}(\omega, p)$, at the interface.[65–67]

Fig. 8 indicates that the vibrational densities of states do not depend on the polarizibility of the metal or liquid phase. Differences in the interfacial thermal conductance, G_{ab}, therefore are likely to arise from changes in the phonon transmission probability, τ_{ab}, between the metal and water, which is strongly influenced by intermolecular forces at the surface. τ_{ab} is sensitive to the details of molecular ordering and interatomic spacing at the interface. Fluctuations in how molecules pack at the surface will therefore alter the conductance (and the temperature gap) at the interface, leading to large fluctuations in the computed value of G.

Our data also indicates that a polarizable metal surface does alter the water ordering adjacent to the surface relative to a non-polarizable metal. This results in a larger population of OH bonds pointing directly at the interface. This effect, in concert with image charge and image dipole interactions present in DR-EAM, is likely to be the cause of the enhanced thermal conductance at the interface. The polarizability of the solvent, however, appears to play very little role in the thermal transport at the metal / water interface. Although TIP4P-FQ has a significantly different bulk thermal conductivity than TIP4P, the interfacial conductance values at the gold interface are the same as each other (within our ability to distinguish).

V. Data Availability

The data that supports the findings of this study are available within the article and its supplementary material and are also available from the corresponding author upon request.

VI. Supplementary Material

See supplementary material for the length dependence for the bulk thermal conductivity of water, additional orientational distributions for water molecules near the surface, difference maps

of these orientational preferences, and vibrational densities of states for all of the systems studied in this paper.

Acknowledgments

Support for this project was provided by the National Science Foundation under Grants CHE-1663773 and CHE-1954648. Computational time was provided by the Center for Research Computing (CRC) at the University of Notre Dame.

References

[1]M. S. Daw and M. I. Baskes, "Embedded-atom method: Derivation and Application to Impurities, Surfaces, And Other Defects in Metals," Phys. Rev. B **29**, 6443–6453 (1984).

[2]S. M. Foiles, M. I. Baskes, and M. S. Daw, "Embedded-atom-method functions for the fcc metals Cu, Ag, Au, Ni, Pd, Pt, and their alloys," Phys. Rev. B **33**, 7983 (1986).

[3]R. A. Johnson, "Alloy models with the embedded-atom method," Phys. Rev. B **39**, 12554 (1989).

[4]M. S. Daw, "Model of metallic cohesion: The Embedded-Atom Method," Phys. Rev. B **39**, 7441–7452 (1989).

[5]S. J. Plimpton and B. A. Hendrickson, "Parallel molecular dynamics with the embedded atom method," in *Materials Theory and Modelling*, MRS Proceedings, Vol. 291, edited by J. Broughton, P. Bristowe, and J. Newsam (Materials Research Society, Pittsburgh, Pa, 1993) p. 37.

[6]A. F. Voter, "The Embedded-Atom Method," in *Intermetallic Compounds: Principles and Practice*, Vol. 1, edited by J. H. Westbrook and R. L. Fleischer (John Wiley and Sons Ltd, 1995) Chap. 4, pp. 77–90.

[7]J. Lu and J. A. Szpunar, "Applications of the embedded-atom method to glass formation and crystallization of liquid and glass transition-metal nickel," Phil. Mag. A **75**, 1057–1066 (1997).

[8]M. M. G. Alemany, C. Rey, and L. J. Gallego, "Transport coefficients of liquid transition metals: A computer simulation study using the embedded atom model," J. Chem. Phys. **109**, 5175–5176 (1998).

[9]M. W. Finnis and J. E. Sinclair, "A simple empirical N-body potential for transition-metals," Philos. Mag. A **50**, 45–55 (1984).

[10]A. P. Sutton and J. Chen, "Long-range Finnis Sinclair potentials," Phil. Mag. Lett. **61**, 139–146 (1990).

[11]M. I. Baskes and R. A. Johnson, "Modified embedded-atom potentials for hcp metals," Model. Simul. Mater. Sci. Eng. **2**, 147–163 (1994).

[12]B. J. Lee and M. I. Baskes, "Second nearest-neighbor modified embedded-atom-method potential," Phys. Rev. B **62**, 8564–8567 (2000).

[13]B. J. Thijsse, "Relationship between the modified embedded-atom method and Stillinger-Weber potentials in calculating the structure of silicon," Phys. Rev. B **65**, 195207 (2002).

[14]M. Timonova and B. J. Thijsse, "Optimizing the meam potential for silicon," Model. Simul. Mater. Sci. Eng. **19**, 015003 (2011).

[15]B. J. Lee, M. I. Baskes, H. Kim, and Y. K. Cho, "Second nearest-neighbor modified embedded atom method potentials for bcc transition metals," Phys. Rev. B **64**, 184102 (2001).

[16]P. van Beurden, H. G. J. Verhoeven, G. J. Kramer, and B. J. Thijsse, "Atomistic potential for adsorbate/surface systems: CO on Pt," Phys. Rev. B **66**, 235409 (2002).

[17]Y. Kimura, Y. Qi, T. Çağin, and W. A. Goddard III, "The Quantum Sutton-Chen many body potential for properties of FCC metals," (1998), downloaded from http://wag.caltech.edu/home-pages/tahir/psfiles/51.ps.

[18]Y. Qi, T. Çağin, Y. Kimura, and W. A. Goddard III, "Molecular-dynamics simulations of glass formation and crystallization in binary liquid metals: Cu-Ag and Cu-Ni," Phys. Rev. B **59**, 3527–3533 (1999).

[19]Y. Chui and K. Chan, "Analyses of surface and core atoms in a platinum nanoparticle," Phys. Chem. Chem. Phys. **5**, 2869–2874 (2003).

[20]G. Wang, M. Van Hove, P. Ross, and M. Baskes, "Surface structures of cubo-octahedral Pt-Mo catalyst nanoparticles from Monte Carlo simulations," J. Phys. Chem. B **109**, 11683–11692 (2005).

[21]B. Medasani, Y. H. Park, and I. Vasiliev, "Theoretical study of the surface energy, stress, and lattice contraction of silver nanoparticles," Phys. Rev. B **75**, 235436 (2007).

[22]A. B. Belonoshko, R. Ahuja, O. Eriksson, and B. Johansson, "Quasi *ab initio* molecular dynamic study of Cu melting," Phys. Rev. B **61**, 3838–3844 (2000).

[23]S. K. R. S. Sankaranarayanan, V. R. Bhethanabotla, and B. Joseph, "Molecular dynamics simulation study of the melting and structural evolution of bimetallic Pd-Pt nanowires," Phys. Rev. B **74**, 155441 (2006).

[24]S. K. R. S. Sankaranarayanan, V. R. Bhethanabotla, and B. Joseph, "Molecular dynamics simulation study of the melting of Pd-Pt nanoclusters," Phys. Rev. B **71**, 195415 (2005).

[25]V. Shastry and D. Farkas, "Molecular statics simulation of fracture in alpha-iron," Model. Simul. Mater. Sci. Eng. **4**, 473–492 (1996).

[26]V. Shastry and D. Farkas, "Atomistic simulation of fracture in CoAl and FeAl," Intermetallics **6**, 95–104 (1998).

[27]C. S. Becquart, D. Kim, J. A. Rifkin, and P. C. Clapp, "Fracture properties of metals and alloys from molecular-dynamics simulations," Mater. Sci. Eng. A. **170**, 87–94 (1993).

[28]T. Shibata, B. A. Bunker, Z. Zhang, D. Meisel, C. F. Vardeman II, and J. D. Gezelter, "Size-dependent spontaneous alloying of Au – Ag nanoparticles," J. Am. Chem. Soc. **124**, 11989–11996 (2002).

[29]R. A. Johnson, "Analytic nearest-neighbor model for fcc metals," Phys. Rev. B **37**, 3924–3931 (1988).

[30]J. A. Rifkin, C. S. Becquart, D. Kim, and P. C. Clapp, "Dislocation generation and crack propagation in metals examined in molecular dynamics simulations," MRS Proceedings **278**, 173 (1992).

[31]Y. Mishin, D. Farkas, M. J. Mehl, and D. A. Papaconstantopoulos, "Interatomic potentials for monoatomic metals from experimental data and *ab initio* calculations," Phys. Rev. B **59**, 3393–3407 (1999).

[32]Y. Mishin, M. J. Mehl, D. A. Papaconstantopoulos, A. F. Voter, and J. D. Kress, "Structural stability and lattice defects in copper: *Ab initio*, tight-binding, and embedded-atom methods," Phys. Rev. B **63**, 224106 (2001).

[33]Y. Mishin, M. J. Mehl, and D. A. Papaconstantopoulos, "Embedded-atom potential for B2-NiAl," Phys. Rev. B **65**, 224114 (2002).

[34]R. R. Zope and Y. Mishin, "Interatomic potentials for atomistic simulations of the Ti – Al system," Phys. Rev. B **68**, 024102 (2003).

[35]Y. Mishin, M. Mehl, and D. Papaconstantopoulos, "Phase stability in the Fe – Ni system: Investigation by first-principles calculations and atomistic simulations," Acta Mat. **53**, 4029–4041 (2005).

[36]X. Zhou, H. Wadley, R. Johnson, D. Larson, N. Tabat, A. Cerezo, A. Petford-Long, G. Smith, P. Clifton, R. Martens, and T. Kelly, "Atomic scale structure of sputtered metal multilayers," Acta Materialia **49**, 4005 – 4015 (2001).

[37]X. W. Zhou, R. A. Johnson, and H. N. G. Wadley, "Misfit-energy-increasing dislocations in vapor-deposited CoFe/NiFe multilayers," Phys. Rev. B **69**, 144113 (2004).

[38]F. H. Streitz and J. W. Mintmire, "Electrostatic potentials for metal-oxide surfaces and interfaces," Phys. Rev. B **50**, 11996–12003 (1994).

[39]S. W. Rick, S. J. Stuart, and B. J. Berne, "Dynamical fluctuating charge force fields: Application to liquid water," J. Chem. Phys. **101**, 6141–6156 (1994).

[40]S. W. Rick, S. J. Stuart, J. S. Bader, and B. J. Berne, "Fluctuating charge force-fields for aqueous-solutions," J. Mol. Liq. **65-6**, 31–40 (1995).

[41]S. W. Rick and S. J. Stuart, "Potentials and algorithms for incorporating polarizability in computer simulations," in *Reviews In Computational Chemistry*, Vol. 18, edited by K. B. Lipkowitz and D. B. Boyd (Wiley-VCH, Inc, 605 Third Ave, New York, NY 10158-0012 USA, 2002) pp. 89–146.

[42]B. Devine, T.-R. Shan, Y.-T. Cheng, A. J. H. McGaughey, M. Lee, S. R. Phillpot, and S. B. Sinnott, "Atomistic simulations of copper oxidation and Cu/Cu_2O interfaces using charge-optimized many-body potentials," Phys. Rev. B **84**, 125308 (2011).

[43]S. Ogata, H. Iyetomi, K. Tsuruta, F. Shimojo, R. K. Kalia, A. Nakano, and P. Vashishta, "Variable-charge interatomic potentials for molecular-dynamics simulations of TiO_2," J. Appl. Phys. **86**, 3036–3041 (1999).

[44]B. Jeon, S. K. Sankaranarayanan, and S. Ramanathan, "Atomistic modeling of ultrathin surface oxide growth on a ternary alloy: Oxidation of Al-Ni-Fe," J. Phys. Chem. C **115**, 6571–6580 (2011).

[45]X. W. Zhou, H. N. G. Wadley, J. S. Filhol, and M. N. Neurock, "Modified charge transfer-embedded atom method potential for metal metal oxide systems," Phys. Rev. B **69**, 035402 (2004).

[46]H. Bhattarai, K. E. Newman, and J. D. Gezelter, "Polarizable potentials for metals: The density readjusting embedded atom method (DR-EAM)," Phys. Rev. B **99**, 094106 (2019).

[47]K. M. Stocker and J. D. Gezelter, "Simulations of heat conduction at thiolate-capped gold surfaces: The role of chain length and solvent penetration," J. Phys. Chem. C **117**, 7605–7612 (2013).

[48]S. M. Neidhart and J. D. Gezelter, "Thermal transport is influenced by nanoparticle morphology: A molecular dynamics study," J. Phys. Chem. C **122**, 1430–1436 (2018).

[49]S. M. Neidhart and J. D. Gezelter, "Thermal conductivity of gold–phenylethanethiol ($Au_{144}PET_{60}$) nanoarrays: A molecular dynamics study," J. Phys. Chem. C **124**, 3389–3395 (2020).

[50]A. Rajabpour, R. Seif, S. Arabha, M. M. Heyhat, S. Merabia, and A. Hassanali, "Thermal transport at a nanoparticle-water interface: A molecular dynamics and continuum modeling study," J. Chem. Phys. **150**, 114701 (2019).

[51]C. J. Fennell and J. D. Gezelter, "Is the Ewald summation still necessary? Pairwise alternatives to the accepted standard for long-range electrostatics," J. Chem. Phys. **124**, 234104 (2006).

[52]R. P. Iczkowski and J. L. Margrave, "Electronegativity," J. Am. Chem. Soc. **83**, 3547–3551 (1961).

[53]H. J. C. Berendsen, J. R. Grigera, and T. P. Straatsma, "The missing term in effective pair potentials," J. Phys. Chem. **91**, 6269–6271 (1987).

[54]W. L. Jorgensen, J. Chandrasekhar, J. D. Madura, R. W. Impey, and M. L. Klein, "Comparison of simple potential functions for simulating liquid water," J. Chem. Phys. **79**, 926–935 (1983).

[55]Y. Dou, L. V. Zhigilei, N. Winograd, and B. J. Garrison, "Explosive boiling of water films adjacent to heated surfaces: A microscopic description," J. Phys. Chem. A **105**, 2748–2755 (2001).

[56]G. Mie, "Zur kinetischen theorie der einatomigen körper," Annalen der Physik **316**, 657–697 (1903).

[57]R. Kubo, "Statistical-mechanical theory of irreversible processes. I. general theory and simple applications to magnetic and conduction problems," J. Phys. Soc. Jpn. **12**, 570–586 (1957).

[58]F. Müller-Plathe, "A simple nonequilibrium molecular dynamics method for calculating the thermal conductivity," J. Chem. Phys. **106**, 6082–6085 (1997).

[59]S. Kuang and J. D. Gezelter, "Velocity shearing and scaling RNEMD: a minimally perturbing method for simulating temperature and momentum gradients," Mol. Phys. **110**, 691–701 (2012).

[60]T. Wei, Y. Li, J. Cheng, and C. Jia, "Finite-size effect of the thermal conductivity in one dimensional chain," New Journal of Physics **21**, 123003 (2019).

[61]M. L. V. Ramires, C. A. Nieto de Castro, Y. Nagasaka, A. Nagashima, M. J. Assael, and W. A. Wakeham, "Standard reference data for the thermal conductivity of water," Journal of Physical and Chemical Reference Data **24**, 1377–1381 (1995).

[62]F. Römer, A. Lervik, and F. Bresme, "Nonequilibrium molecular dynamics simulations of the thermal conductivity of water: A systematic investigation of the SPC/E and TIP_4P/2005 models," The Journal of Chemical Physics **137**, 074503 (2012).

[63]T. W. Sirk, S. Moore, and E. F. Brown, "Characteristics of thermal conductivity in classical water models," The Journal of Chemical Physics **138**, 064505 (2013).

[64]K. M. Stocker, S. M. Neidhart, and J. D. Gezelter, "Interfacial thermal conductance of thiolate-protected gold nanospheres," J. Appl. Phys. **119**, 025106 (2016), http://dx.doi.org/10.1063/1.4939956.

[65]E. T. Swartz and R. O. Pohl, "Thermal Boundary Resistance," Rev. Mod. Phys. **61**, 605–668 (1989).

[66]P. Reddy, K. Castelino, and A. Majumdar, "Diffuse Mismatch Model of Thermal Boundary Conductance using Exact Phonon Dispersion," Appl. Phys. Lett. **87**, 211908 (2005).

[67]C. Monachon, L. Weber, and C. Dames, "Thermal Boundary Conductance :A Materials Science Perspective," Annu. Rev. Mater. Res. **8**, 1–31 (2016).